Study on the Damage Behavior of Engineered Cementitious Composites: Experiment, Theory, and Numerical Implementation

Tingting Ding [1], Zhuo Wang [1], Yang Liu [1], Xinlong Wang [2], Tingxin Sun [2] and Shengyou Yang [2,*]

1 Shandong Provincial Communications Planning and Design Institute Group Co., Ltd., Jinan 250101, China; sjy_yfzx_tding@163.com (T.D.); sjy_yfzx_zwang@163.com (Z.W.); sjy_yfzx_yliu@163.com (Y.L.)
2 School of Civil Engineering, Shandong University, Jinan 250061, China; 202214995@mail.sdu.edu.cn (X.W.); 202235070@mail.sdu.edu.cn (T.S.)
* Correspondence: syang_mechanics@sdu.edu.cn

Abstract: The ever-increasing material performance requirements in modern engineering structures have thrust engineered cementitious composites (ECCs) into the limelight of civil engineering research. The exceptional tensile, bending, and crack-control abilities of ECCs have sparked significant interest. However, the current research on the mechanical behavior of ECCs primarily focuses on uniaxial tensile and compressive constitutive relationships, leaving a gap in the form of a comprehensive multidimensional constitutive model that can fully describe its complex behavior at large strains. This study rigorously addresses this gap by initially investigating the uniaxial tensile and compressive behavior of ECCs through experiments and establishing a one-dimensional constitutive relationship of ECCs. It then introduces the concepts of damage energy release rate and energy equivalent strain, and constructs a three-dimensional constitutive model of ECCs by introducing the damage variable function. We write the numerical algorithm of our theoretical model in terms of the VUMAT subroutine and implement it into ABAQUS 2019 finite element software. We validate the accuracy and practicality of the multidimensional constitutive model by comparing the experimental data of uniaxial tension/compression and four-point bending. This paper enriches the theoretical system of ECCs and provides rigorous guidance for the performance optimization and practical application of such advanced engineering materials.

Keywords: engineered cementitious composites (ECCs); high ductility; material damage; constitutive model; numerical implementation

1. Introduction

Concrete is a widely used civil engineering material. Its future development in infrastructure construction lies in green and low-carbon strategies and extreme engineering environments. To address concrete's limitations, material additives are commonly used to enhance its tensile strength, ensuring the durability and safety of concrete structures [1].

Traditional concrete is widely used in various structural engineering applications due to its relatively low construction and maintenance costs and its excellent durability and workability. However, conventional concrete, with its low tensile strength, is prone to cracking, and once damaged, it completely loses its load-bearing capacity, significantly affecting its performance. Many scholars have incorporated various fibers into concrete to address these issues to improve its durability and toughness [2–6]. Li and his collaborators developed polyvinyl alcohol (PVA) fiber-reinforced cement-based composites in the exploration process and studied their high performances experimentally and theoretically [7–10]. Subsequently, with in-depth research and continuous optimization of material properties, fiber-reinforced concrete [11,12], standard high-performance fiber-reinforced concrete [13–15], and high-ductility fiber-reinforced cementitious composites [16–21] were successively born.

In general, engineered cementitious composites (ECCs) use short PVA fibers for reinforcement, with a fiber content volume ratio of about 2%. Its characteristics are high ductility, high toughness, tensile hardening, and fine crack density [22]. The ultimate tensile strain can reach more than 3%, effectively overcoming the defect of brittle cracking in ordinary cement-based materials [23]. In addition, ECCs have shown excellent performance in resistance to impact [24], fatigue [25], freeze–thaw cycles [26], corrosion [27], and wear resistance, and also have good self-healing properties [28]. These characteristics give ECCs broad application prospects in civil engineering, offering new solutions to improve the safety and durability of building structures [29].

The current research on ECCs mainly involves experimental studies of uniaxial tensile and compressive properties, as well as constitutive modeling [30], the analysis of the effects of different ratios and additives on the properties [31], as well as the evaluation of the performance of ECCs and the discussion of the engineering applications [32], which gradually deepens the understanding of the properties of ECCs. Compared to regular concrete, ECCs are known for exceptional tensile properties, making these a focal point of research. Currently, various uniaxial tensile constitutive models for ECCs have been proposed. From the macroscopic mechanical properties, researchers have successively proposed the trilinear hardening model [7], the bifold hardening model [33], and the improved bilinear hardening model [34], etc. Chen et al. [35] presented a biaxial constitutive model of ECCs, considering the biaxial mechanical behavior of concrete. While these models can accurately describe the nonlinear characteristics of the stress–strain relationship, they struggle to accurately reflect the damage of ECCs due to the development of microcracks.

On the other hand, starting from the microscopic point of view, scholars have established microscopic models based on fracture mechanics to consider the fiber-bridging effect to develop the uniaxial tensile intrinsic model [36] and to evaluate the effect of initial defects on the tensile properties of ECCs [37]. However, these models can only describe the uniaxial model, which cannot be applied to engineering scenarios that include more complicated stress conditions.

To fully elucidate the stress behavior of ECCs, particularly the damage evolution law, researchers have incorporated damage mechanics methods into the investigation of ECC tensile constitutive models. For example, Krahl et al. [38] defined the damage factor based on the tensile and compressive damage evolution law of ultra-high performance fiber-reinforced concrete by using the stiffness method. Cai et al. [39] also defined the damage factor for ECCs using the stiffness method, while Cheng et al. [40] used the Najar energy method to determine the tensile and compressive damage factors of ECCs. The aforementioned models have an excessive number of fitting parameters, which impedes the widespread application of ECCs in engineering practice. Therefore, it is crucial to thoroughly investigate the damage mechanism of ECCs to establish a more accurate and practical ECCs constitutive model.

This article examines the monotonic load test data of ECCs, introduces damage variables using the stiffness method, and first establishes a simple and physically meaningful uniaxial tensile constitutive model of ECCs. We then construct a three-dimensional constitutive model of ECCs using energy release rate and energy equivalent strain. We write the numerical algorithm into the ABAQUS software through the VUMAT subroutine and compare the numerical results with the uniaxial and four-point bending experimental data. This theoretical model and its numerical implementation effectively promote the widespread application of ECCs in engineering practice, furthering their development in civil engineering.

2. Establishment of a Constitutive Model for ECCs

2.1. Uniaxial Compression

2.1.1. Experiments

ECC raw materials include cement, fly ash, tailings sand, quartz sand, thickener, water, water-reducing agent, and fiber. The cement grade is P.O. 42.5, and the fly ash is

grade I. The particle size of quartz sand is 80–120 mesh. The thickener is 150,000 viscosity hydroxypropyl methylcellulose, and the water-reducing agent is a polycarboxylate series, a high-efficiency water-reducing agent. The fiber is made of domestically produced PVA fiber developed by Shandong Provincial Transportation Planning and Design Institute, and the properties of the fibers are shown in Table 1.The chemical composition of concrete is shown in Table 2, the chemical composition of fly ash is shown in Table 3, and the mix of ECC specimens is shown in Table 4. Perform compressive strength tests on ECC specimens with different proportions and dimensions of 70.7 mm × 70.7 mm × 70.7 mm. The specimen diagram and test diagram are shown in Figure 1.

Table 1. Selection of uniaxial compression constitutive parameters.

Length (mm)	Diameter (μm)	Elastic Modulus (GPa)	Tensile Strain (%)	Tensile Strength (MPa)	Density (g/cm^3)
12	40	39.5	7.0	1650	1.3

Table 2. Chemical composition of cement.

Chemical Composition	CaO	SiO$_2$	Al$_2$O$_3$	Fe$_2$O$_3$	SO$_3$	MgO	K$_2$O	MnO
Content (%)	63.21	18.48	6.74	3.45	3.16	3.24	0.53	0.27

Table 3. Chemical composition of fly ash.

Chemical Composition	SiO$_2$	Al$_2$O$_3$	Fe$_2$O$_3$	CaO	SO$_3$
Content (%)	45.05%	21.97	7.76	17.64	1.46

Table 4. The mix proportion and maintenance time of ECC.

Cement	Fly Ash	Quartz Sand	Water Cement Ratio	Fiber Content/%	Curing Time (Days)
1	1.2	0.8	0.28	2.0	28

The testing machine is the WDW-300 microcomputer-controlled electronic universal testing machine manufactured by ZHONGSHISTRENCH Company, Jinan, China.

2.1.2. Model Establishment

The difference in compressive strength between ECCs and ordinary concrete is insignificant. Still, due to the absence of coarse aggregates, the elastic modulus of ECCs is much lower than that of ordinary concrete, about 20 MPa to 25 MPa. Its uniaxial compression behavior is almost the same as that of ordinary concrete. Figure 2a shows the constitutive model of concrete under uniaxial compression, given in the "Code for Design of Concrete Structures" (GB 50010-2010) [41] (from now on referred to as the code), and Figure 2b shows the ECCs uniaxial compression test curve obtained according to the "Standard Test Methods for Physical and Mechanical Properties of Concrete" (GB-T 50081-2019) [42].

Figure 1. ECC uniaxial compression test: (**a**) 70.7 mm × 70.7 mm × 70.7 mm cubic specimen; (**b**) specimen loading diagram.
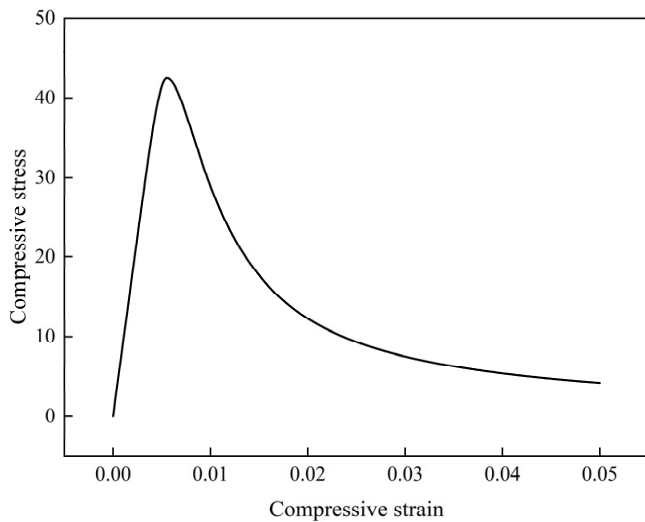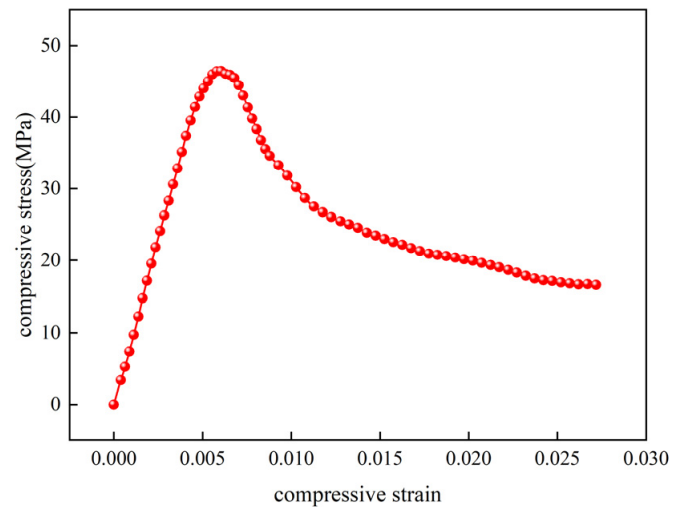
Figure 2. Uniaxial compressive stress–strain curve: (**a**) concrete; (**b**) ECCs.

The constitutive model of damage mechanics can be divided into isotropic damage constitutive models based on the different types of damage:

$$\boldsymbol{\sigma} = (1 - D)\widetilde{\boldsymbol{\sigma}} \qquad (1)$$

The anisotropic damage constitutive model is as follows [43]:

$$\boldsymbol{\sigma} = (\mathbb{I} - \mathbb{D}) : \widetilde{\boldsymbol{\sigma}} \qquad (2)$$

where $\mathbb{D} = \left\{ D_{ijkl} \right\}$ is the damage tensor and $\widetilde{\sigma}$ is the effective stress tensor.

For concrete materials, the damage caused by tension and compression is different. Ladevèze [44] and Mazars [45] believe that after decomposing concrete into positive and negative stresses, it can be assumed that tensile damage is only caused by tensile stress, and compressive damage is only caused by compressive stress. Based on this, uniaxial equivalent strain is defined, and an isotropic damage model for concrete materials is established. That is to say, compressive stress and tensile stress can be considered to cause isotropic damage to the concrete material. Therefore, for the uniaxial tension–compression state, a single scalar damage model is used to describe its damage.

Figure 2 shows that the uniaxial compressive behavior of ECCs is similar to the shape of the constitutive relationship given in the specifications. The stress–strain relationship can be written as

$$\sigma = (1 - d_c)E_c\varepsilon \tag{3}$$

where d_c is the damage variable under uniaxial compression, and E_c is Young's modulus of the linear elastic segment. The explicit form of d_c is given by [42]:

$$d_c = \begin{cases} 1 - \dfrac{\rho_c n_c}{n_c - 1 + x^{n_c}} & x \leq 1 \\ 1 - \dfrac{\rho_c}{\alpha_c(x-1)^{\gamma_c} + x} & x > 1 \end{cases} \tag{4}$$

where $x = \frac{\varepsilon}{\varepsilon_{cr}}$, $\rho_c = \frac{\sigma_{cr}}{E_c\varepsilon_{cr}}$, $n_c = \frac{E_c\varepsilon_{cr}}{E_c\varepsilon_{cr} - \sigma_{cr}}$, and σ_{cr} is the peak stress of the compression curve, ε_{cr} is the strain corresponding to the peak stress, α_c and γ_c are undetermined parameters. Ferretti [46] provided an effective method for determining the damage variable by using an experimental procedure. In contrast, the method used in this article is to use Matlab 2019a to fit formulas with experimental data.

During the softening stage, the secant stiffness of ECCs decreases slower than that of ordinary concrete. Therefore, the constitutive relationship in the specification is selected as the constitutive relationship for ECCs under uniaxial compression, and it is improved by introducing parameters γ_c to control the shape near the peak of the curve and the secant stiffness during the descent phase.

2.1.3. Model Validation

ECCs with a fly ash ratio of 0.27, PVA fiber ratio of 1.5%, quartz sand of 0.508, water reducing agent of 0.015, water cement ratio of 0.36, and sand cement ratio of 0.40 were selected for the experiment. The parameters were obtained based on the stress–strain curve of the test data, as shown in Table 5. The values of α_c and γ_c were fitted from experimental data, with a correlation coefficient of r = 0.99.

Table 5. Selection of uniaxial compression constitutive parameters.

σ_{cr} (MPa)	ε_{cr}	E (MPa)	α_c	γ_c
46.45	0.006042	9027.63	1.391	1.443

We substitute the parameters from Table 5 into Equations (1) and (2) to obtain the theoretical curve of the uniaxial compression constitutive model and fit it with the experimental data. The results are depicted in Figure 3.

When we analyze Figure 3, we observe that the constitutive model's stress peak and corresponding strain align with the experimental data. Prior to reaching the peak, the model's stiffness matches the experimental data. During the softening stage, the parameter γ_c leads to a similar rate of stiffness decrease between the constitutive model and experimental data.
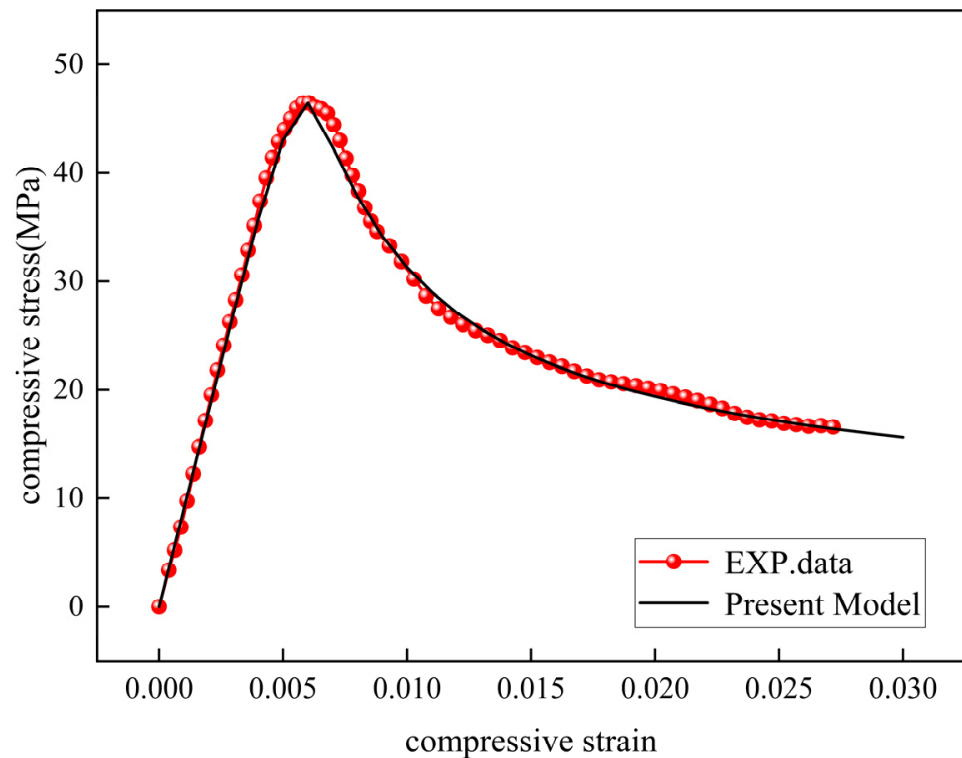
Figure 3. Uniaxial tensile theoretical curves fitted to experimental data.

2.2. Uniaxial Tension

2.2.1. Experiments

Select the same raw materials as the uniaxial compression test and conduct a tensile test. Prepare uniaxial tensile test data of 330 mm × 60 mm × 13 mm dog bone specimens of ECCs with different ratios and test the tensile strength. The schematic diagram and experimental process diagram of the experiment are shown in Figure 4.

2.2.2. Model Establishment

The behavior of ECC materials under tension significantly differs from the constitutive relationship provided by the specifications. Figure 5a illustrates the uniaxial tensile constitutive model of concrete materials as per the specifications, resembling the uniaxial compressive model and comprising linear elastic, nonlinear, and post-peak decreasing stages. Figure 5b displays the stress–strain curve of ECCs under uniaxial compression obtained from experiments. A comparison of the two figures reveals that the specified constitutive relationship is not suitable for describing the mechanical behavior of ECCs under tension. Consequently, it is necessary to analyze the uniaxial tensile test data for ECCs and reconstruct the constitutive model for tension.

Based on the characteristics of the uniaxial tension curve of the ECCs, a double-line model is used to establish the stress–strain relationship, such as

$$\sigma = (1 - d_t)E_t\varepsilon \tag{5}$$

Here, the uniaxial tensile damage variable d_t is expressed as

$$d_t = \begin{cases} 1 - \frac{\rho_t n_t}{n_t - 1 + x^{n_t}} & x \leq 1 \\ 1 - \rho_m + \frac{\rho_m - \rho_t}{x} & x > 1 \end{cases} \tag{6}$$

where $x = \frac{\varepsilon}{\varepsilon_{tr}}$, $\rho_t = \frac{\sigma_{tr}}{E_t\varepsilon_{tr}}$, $\rho_m = \frac{\sigma_{tp} - \sigma_{tr}}{E_t(\varepsilon_{tp} - \varepsilon_{tr})}$, $n_t = \frac{E\varepsilon_{tr}}{E\varepsilon_{tr} - \sigma_{tr}}$, and σ_{tr} is the stress at the stage of failure, ε_{tr} is the strain at the stage of failure, σ_{tp} is the stress at failure, ε_{tp} is the strain at failure.
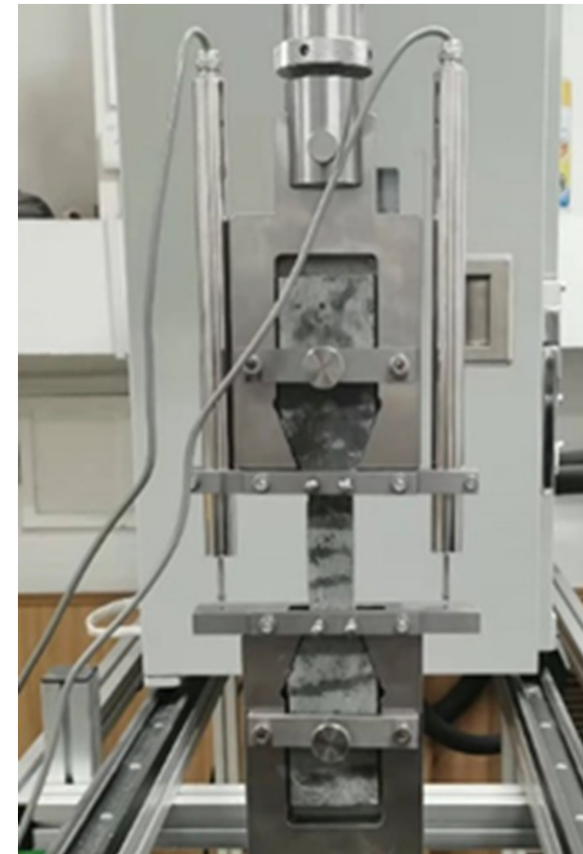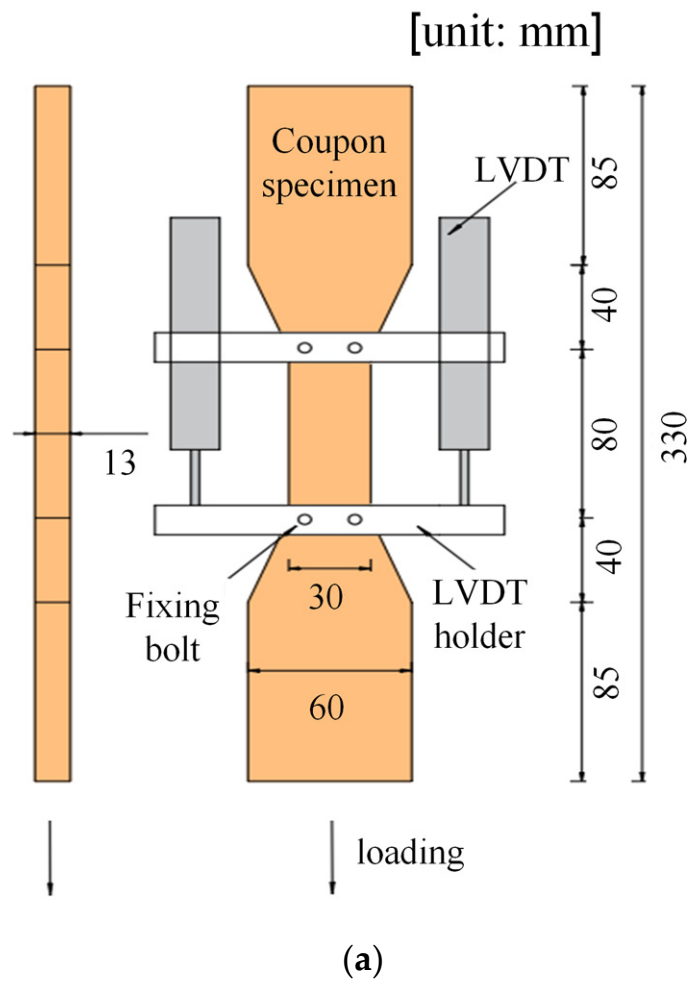
Figure 4. ECCs uniaxial tensile test: (**a**) schematic diagram; (**b**) fixture diagram.
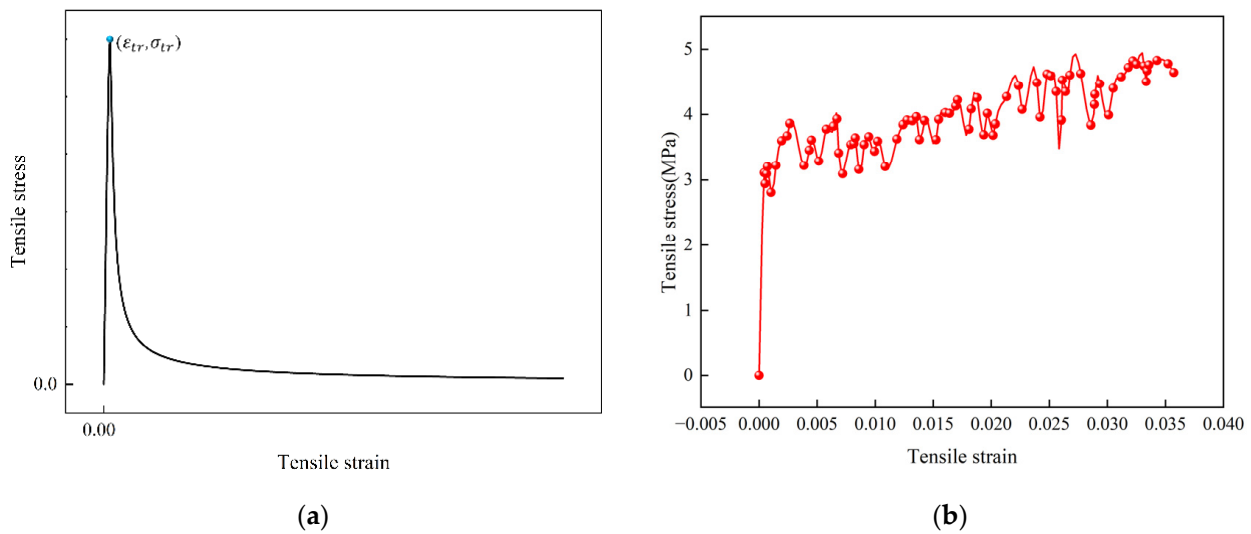
Figure 5. Uniaxial tensile stress–strain curves: (**a**) concrete; (**b**) ECCs.

2.2.3. Model Validation

ECCs were chosen for the experiment with a 100% quartz sand replacement rate, 0% tailings sand replacement rate, and 2.0% REC-15 PVA fiber content. The necessary parameters for the constitutive relationship were derived from the stress–strain curve of the experimental data, as depicted in Table 6.

Table 6. Selection of uniaxial tensile constitutive parameters.

σ_{tr} (MPa)	ε_{tr}	σ_{tp} (MPa)	ε_{tr}	E_t (MPa)
3.11205	0.00045242	4.49894	0.0333467	9027.63

Substitute the parameters into Equation (4) to obtain the constitutive model. Then, it will be fitted with the experimental data and generated in Figure 6.

In Figure 6, the inflection points of the current model align with the dense crack stage, and the slopes of the stress–strain curves at this stage are well-matched. However, a significant drawback of the model is the absence of a distinct failure point. Even after reaching the predetermined failure strain, the stress–strain relationship exhibits a linear growth trend, which differs substantially from the actual material behavior after damage.

To accurately depict the mechanical properties of materials, it is imperative to enhance the current model and incorporate a failure mechanism to ensure that it accurately represents the failure state of materials after reaching the failure strain. After making the necessary corrections, the uniaxial tensile damage variable is obtained as

$$d_t = \begin{cases} 1 - \dfrac{\rho_t n_t}{n_t - 1 + x^{n_t}} & x \leq 1 \\ 1 - \rho_m + \dfrac{\rho_m - \rho_t}{x} & 1 < x < \dfrac{\varepsilon_{tp}}{\varepsilon_{tr}} \\ 1 & x \geq \dfrac{\varepsilon_{tp}}{\varepsilon_{tr}} \end{cases} \tag{7}$$

and the fitting result is shown in Figure 7.

As shown in Figure 7, when the tensile strain reaches the failure strain, the element's stiffness decreases to zero, consistent with the actual situation. The failure criteria have been revised.
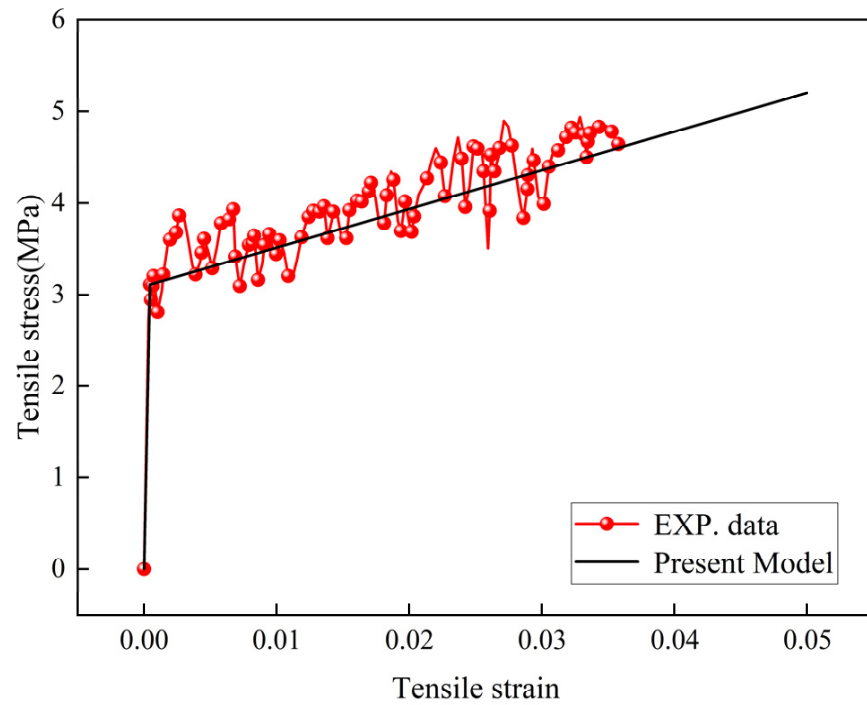
Figure 6. Uniaxial tensile constitutive model fitted to the experimental data.
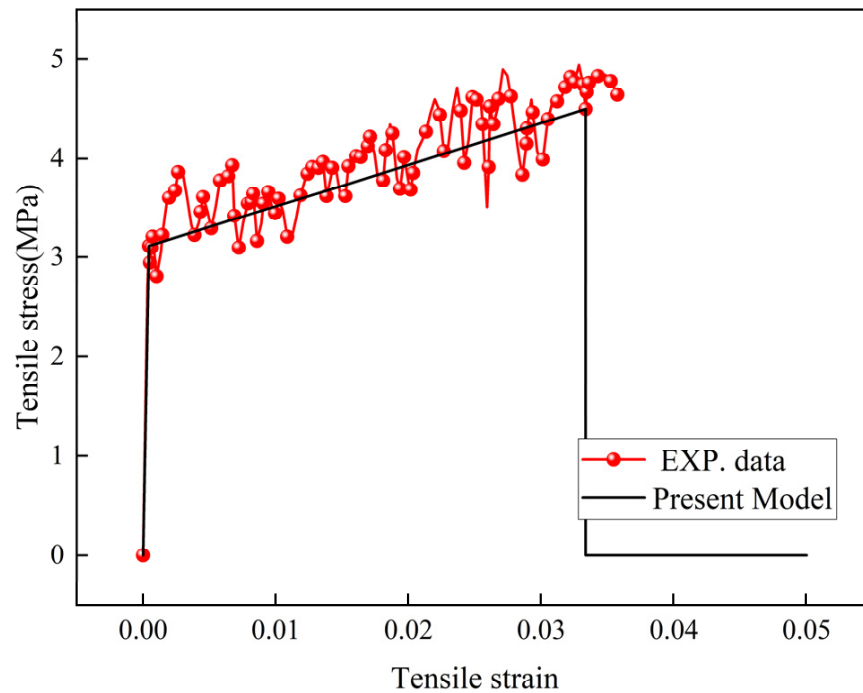
Figure 7. Modified uniaxial tensile constitutive model fitted to the experimental data.

2.3. Three-Dimensional Model

The constitutive relationship of concrete under biaxial stress includes incremental and complete forms. It can be used in complex situations such as unloading and repeated loading. However, it requires a relatively large number of parameters and needs re-fitting for different stress ratios. Constitutive relationships under triaxial stress are even more complex, with more factors and parameters to consider.

We aim to use a one-dimensional damage constitutive relationship to simplify establishing a multidimensional constitutive model and reduce the number of parameters.

This involves analyzing stress states and their influence on different loading directions to derive the damage variable in the main direction. This method simplifies the model complexity and accurately describes concrete's mechanical behavior under multi-dimensional stress states.

2.3.1. Principal Stresses and Strains

In a three-dimensional Cartesian coordinate system, the stress state at any point in a continuous medium can be expressed as a second-order tensor $\boldsymbol{\sigma} = \sigma_{ij}\boldsymbol{e}_i \otimes \boldsymbol{e}_j$ and the subscripts i and j range from 1 to 3. The basis vectors are denoted as $\boldsymbol{e}_i$. The component form of the stress tensor is given by

$$\boldsymbol{\sigma} = \begin{pmatrix} \sigma_{11} & \sigma_{12} & \sigma_{13} \\ \sigma_{21} & \sigma_{22} & \sigma_{23} \\ \sigma_{31} & \sigma_{32} & \sigma_{33} \end{pmatrix} \tag{8}$$

The principal stresses and the corresponding directions are obtained by solving the following equation:

$$|\boldsymbol{\sigma} - \lambda \mathbf{I}| = 0 \tag{9}$$

where λ is the eigenvalue and $\mathbf{I}$ is the second-order identity tensor.

By solving Equation (7), the obtained three eigenvalues are actually the three principal stresses σ_1, σ_2, and σ_3. The principal stress matrix $\boldsymbol{\sigma_p}$ is

$$\boldsymbol{\sigma_p} = \begin{bmatrix} \sigma_1 & & \\ & \sigma_2 & \\ & & \sigma_3 \end{bmatrix} \tag{10}$$

In addition, the corresponding feature vectors are $\boldsymbol{\xi}_i$ (i = 1, 2, 3). Three unit orthogonal eigenvectors $\boldsymbol{\xi}_1, \boldsymbol{\xi}_2, \boldsymbol{\xi}_3$ form the principal direction matrix $\mathbf{Q}$, namely,

$$\mathbf{Q} = (\boldsymbol{\xi}_1, \ \boldsymbol{\xi}_2, \ \boldsymbol{\xi}_3) \tag{11}$$

The state of compression or tension is determined based on the sign of σ_i in Equation (8). For instance, if $\sigma_i < 0$, it means that the i-th principal direction is under compression, and if $\sigma_j > 0$, it means that the j-th principal direction is under tension. The principal stresses, σ_i, are arranged from smallest to largest, and, as a result, the corresponding principal directions are also arranged in the same order. Therefore, if $\sigma_i < 0$ and $\sigma_{(i+1)} > 0$, it indicates that the first i principal directions are all under compression, while the (i + 1)-th and subsequent principal directions are under tension.

Thus, the principal stress tensor can be decomposed into a compressive principal stress tensor $\sigma_{\mathbf{p}}^-$ and a tensile principal stress tensor $\sigma_{\mathbf{p}}^+$, such as

$$\boldsymbol{\sigma_p} = \boldsymbol{\sigma_p}^- + \boldsymbol{\sigma_p}^+ \tag{12}$$

Their matrix forms are expressed as

$$\boldsymbol{\sigma_p}^- = \begin{pmatrix} \sigma_1^- & & \\ & \sigma_2^- & \\ & & \sigma_3^- \end{pmatrix} \tag{13}$$

and

$$\boldsymbol{\sigma_p}^+ = \begin{pmatrix} \sigma_1^+ & & \\ & \sigma_2^+ & \\ & & \sigma_3^+ \end{pmatrix} \tag{14}$$

From the compressive and tensile principal stress tensor, we can decompose the stress tensor to obtain the compressive tensor σ^- and tensile tensor σ^+, whose matrix forms are expressed as

$$\boldsymbol{\sigma}^- = \mathbf{Q}\boldsymbol{\sigma}_{\mathrm{p}}^- \mathbf{Q}^T \text{ and } \boldsymbol{\sigma}^+ = \mathbf{Q}\boldsymbol{\sigma}_{\mathrm{p}}^+ \mathbf{Q}^T \tag{15}$$

In fact, the relationship between stress, tensile stress, and compressive stress can also be expressed as [47]:

$$\boldsymbol{\sigma} = \mathbb{P}^+ : \boldsymbol{\sigma}^+ \text{ and } \boldsymbol{\sigma} = \mathbb{P}^- : \boldsymbol{\sigma}^- \tag{16}$$

Here, $\mathbb{P}^+, \mathbb{P}^-$ are fourth-order projection tensors, and satisfy the relationship:

$$\mathbb{P}^+ + \mathbb{P}^- = \mathbb{I} \tag{17}$$

where $\mathbb{I}$ is the fourth-order identity tensor.

The invariant of the compressive stress tensor is the same as that of the compressive principal stress tensor. Similarly, the invariant of the tensile stress tensor is the same as that of the tensile principal stress tensor.

The first invariant and the second bias stress invariant of $\sigma_p^{\pm}$ are defined as

$$I^{\pm} = \sum_{i=1}^{3} \sigma_i^{\pm} \tag{18}$$

$$J_2^{\pm} = \frac{1}{6}\left((\sigma_1^{\pm} - \sigma_2^{\pm})^2 + (\sigma_2^{\pm} - \sigma_3^{\pm})^2 + (\sigma_3^{\pm} - \sigma_1^{\pm})^2\right) \tag{19}$$

2.3.2. Free Energy

We define the elastic Helmholtz free energy (HFE) in the framework of continuum damage mechanics as

$$\psi_0^e = \frac{1}{2}\boldsymbol{\sigma} : \boldsymbol{\varepsilon}^{\mathbf{e}} = \frac{1}{2}\boldsymbol{\sigma}^- : \boldsymbol{\varepsilon}^{\mathbf{e}} + \frac{1}{2}\boldsymbol{\sigma}^+ : \boldsymbol{\varepsilon}^{\mathbf{e}} = \psi_0^{e-} + \psi_0^{e+} \tag{20}$$

For linearly elastic materials, the stress–strain relation is

$$\boldsymbol{\varepsilon} = \mathbb{C} : \boldsymbol{\sigma} \tag{21}$$

where $\mathbb{C}$ is the fourth-order flexibility tensor.

Given that both compressive and tensile loading can cause a decrease in the overall mechanical properties, we introduce two damage scalars, d^- and d^+, to represent the damage variables in compression and tension, respectively. This allows the post-damage elastic material's HFE to be expressed as

$$\psi^e(\boldsymbol{\varepsilon}^{\mathbf{e}}, d^+, d^-) = \psi^{e-}(\boldsymbol{\varepsilon}^{\mathbf{e}}, d^-) + \psi^{e+}(\boldsymbol{\varepsilon}^{\mathbf{e}}, d^+) \tag{22}$$

In detail, we define the post-damage compressive stress tensor σ_d^- and the tensile stress tensor σ_d^+ as

$$\boldsymbol{\sigma}_d^- = (1 - d^-)\boldsymbol{\sigma}^- \tag{23}$$

$$\boldsymbol{\sigma}_d^+ = (1 - d^+)\boldsymbol{\sigma}^+ \tag{24}$$

Then, the compressed and stretched HFE can be expressed as

$$\psi^{e\pm}(\boldsymbol{\varepsilon}^{\mathbf{e}}, d^{\pm}) = \frac{1}{2}\boldsymbol{\sigma_d}^{\pm} : \boldsymbol{\varepsilon}^{\mathbf{e}} = \frac{1}{2}(1 - d^{\pm})\boldsymbol{\sigma}^{\pm} : \boldsymbol{\varepsilon}^{\mathbf{e}} = (1 - d^{\pm})\psi_0^{e\pm} \tag{25}$$

The presence of plastic strains within the ECCs means that in the case of isothermal adiabatic, the elastic and plastic HFEs are not coupled [48]. This allows the HFE to be decomposed into elastic and plastic components for elastic–plastic materials. When the

material deforms, the strain tensor includes both the elastic strain tensor and the plastic strain tensor, namely

$$\varepsilon = \varepsilon^{\mathbf{e}} + \varepsilon^{\mathbf{p}} \tag{26}$$

Concrete materials behave in a quasi-brittle manner when under tensile stress. However, in the case of ECCs, dense cracks form inside the concrete as it reaches the destructive stage under tension, demonstrating its excellent tensile properties. This is mainly due to the combined tensile action of the fibers and the matrix. Despite this, the matrix part of ECCs still behaves in a quasi-brittle manner. When ECCs are subjected to tension, the effect of plastic deformation is relatively small, so plastic deformation in tension can be disregarded when analyzing the mechanical behavior of ECCs. Therefore, the total elastic-plastic HFE can be expressed as

$$\psi(\varepsilon^{\mathbf{e}}, \kappa, d^+, d^-) = \psi^e(\varepsilon^e, d^+, d^-) + \psi^p(\kappa, d^-) \tag{27}$$

where κ is a suitable set of plasticity variables, and the plasticity HFE can be expressed as

$$\psi^p(\kappa, d^-) = (1 - d^-)\psi_0{}^p = (1 - d^-)\int_0^{\varepsilon^{\mathbf{p}}} \sigma^- : \mathrm{d}\varepsilon^{\mathbf{p}} \tag{28}$$

2.3.3. Damage Dissipation

According to the second law of thermodynamics, every process must adhere to Clausius' inequality, which can be simplified as

$$\dot{\gamma} = -\dot{\psi} + \sigma : \dot{\varepsilon} \geq 0 \tag{29}$$

By substituting Equation (27) into (29), we have

$$\sigma_d^+ : \dot{\varepsilon}^{\mathbf{e}} + \sigma_d^- : \dot{\varepsilon}^{\mathbf{e}} - \frac{\partial \psi^e}{\partial \varepsilon^e} : \dot{\varepsilon}^{\mathbf{e}} + (-\frac{\partial \psi^e}{\partial d^-})\dot{d}^- + (-\frac{\partial \psi^e}{\partial d^+})\dot{d}^+ + (\sigma_d^- : \dot{\varepsilon}^{\mathbf{p}} - \frac{\partial \psi^p}{\partial \kappa} \cdot \dot{\kappa}) \geq 0 \tag{30}$$

From Equation (25), the algebraic sum of the first three terms in Equation (26) is zero. Therefore, to satisfy the laws of thermodynamics, the damage evolution process should satisfy the following two conditions. The first one is the plastic dissipation inequality:

$$\sigma_d^- : \dot{\varepsilon}^{\mathbf{p}} - \frac{\partial \psi^p}{\partial \kappa} \cdot \dot{\kappa} \geq 0 \tag{31}$$

The second one is damage dissipation inequality:

$$(-\frac{\partial \psi^e}{\partial d^-})\dot{d}^- = Y^- \cdot \dot{d}^- \geq 0 \tag{32}$$

and

$$(-\frac{\partial \psi^e}{\partial d^+})\dot{d}^+ = Y^+ \cdot \dot{d}^+ \geq 0 \tag{33}$$

where Y^- and Y^+ are the compressive and tensile damage energy release rates, respectively. In detail, the rates are

$$Y^- = \psi_0{}^{e-} + \psi_0{}^p \tag{34}$$

$$Y^+ = \psi_0{}^{e+} = \frac{1}{2}\sigma^+ : \mathbb{C} : \sigma \tag{35}$$

Equation (31) expresses the elastic HFE, further explored below, regarding concrete's plasticity. The HFE of the initial elastic material is

$$\psi_0{}^{e\pm} = \frac{1}{2}\sigma^{\pm} : \mathbb{C} : \sigma = \frac{1}{2E_0}\{\frac{2(1+\nu)}{3}3J_2{}^{\pm} + \frac{1-2\nu}{3}(I_1{}^{\pm})^2 - \nu I_1{}^+ I_1{}^-\} \tag{36}$$

where $I_1^{\pm}$ and $J_2^{\pm}$ are defined by Equations (14) and (15), respectively.

2.3.4. Evolution Process

In the effective stress space, the evolution laws of plastic strain are expressed as

$$\dot{\boldsymbol{\sigma}} = \mathbb{E} : (\dot{\boldsymbol{\varepsilon}} - \dot{\boldsymbol{\varepsilon}}^{\mathbf{P}}) \tag{37}$$

$$\dot{\varepsilon}^p = \dot{\lambda}^p \frac{\partial F^p(\boldsymbol{\sigma})}{\partial \boldsymbol{\sigma}} \tag{38}$$

$$\dot{\boldsymbol{\kappa}} = \dot{\lambda}^p \boldsymbol{H} \tag{39}$$

$$F(\boldsymbol{\sigma}, \boldsymbol{\kappa}) \leq 0, \ \dot{\lambda}^p \geq 0, \ \dot{\lambda}^p F(\boldsymbol{\sigma}, \boldsymbol{\kappa}) = 0 \tag{40}$$

where $\dot{\lambda}^p$ is the plastic flow factor, $F^P(\boldsymbol{\sigma})$ is the plastic potential function, $\boldsymbol{\kappa}$ is the variable that responds to the plastic hardening process, $F(\boldsymbol{\sigma}, \boldsymbol{\kappa})$ is the plastic yield function, and $\boldsymbol{H}$ is the plastic hardening function. Its form is

$$\mathbf{H} = \frac{\partial \boldsymbol{\kappa}}{\partial \boldsymbol{\varepsilon}^{\mathbf{p}}} : \frac{\partial F^p}{\partial \boldsymbol{\sigma}} \tag{41}$$

The hardening parameter is positively correlated with the plastic strain increment. According to the study by Li Jie et al. [47], the hardening variable can be defined as

$$\boldsymbol{\kappa} = \left\{ \kappa^+, \kappa^- \right\}^T \tag{42}$$

$$\dot{\kappa}^{\pm} = \sqrt{\dot{\varepsilon}^{p\pm} \cdot \dot{\varepsilon}^{p\pm}} = \left| \dot{\varepsilon}^p \right| \tag{43}$$

When only considering linear hardening, the effective stress under tension and compression $\sigma^+(\kappa^+)$, $\sigma^-(\kappa^-)$ can be expressed as

$$\sigma^{\pm}(\kappa^{\pm}) = \sigma_y^{\pm} + E^{p\pm}\kappa^{\pm} \tag{44}$$

where $\sigma_y^{\pm}$ is the yield stress under uniaxial tension and compression, and $E^{p\pm}$ is the effective plastic hardening modulus under uniaxial tension or compression.

According to the research of Lubliner and Lee et al., the form of the plastic potential function should be

$$F^P(\boldsymbol{\sigma}) = \alpha^p I_1 + \sqrt{2J_2} \tag{45}$$

where I_1 is the first invariant of the stress tensor, J_2 is the second bias stress invariant of the stress tensor, and α^p is a parameter reflecting the dilatancy effect of concrete.

According to Lee and Fenves' revised Lubliner, the plastic yield function can be expressed as

$$F(\sigma, \kappa) = (\alpha I_1 + \sqrt{3J_2} + \beta \langle \sigma_{\max} \rangle) - (1 - \alpha)c \leq 0 \tag{46}$$

where $\langle x \rangle = \max(x, 0)$ and α is a constant, namely

$$\alpha = \frac{r - 1}{2r - 1} \tag{47}$$

$$r = \frac{f_{by}^-}{f_y^-} \tag{48}$$

where f_{by}^- is the peak strength under biaxial isobaric pressure, and f_y^- is the peak strength under uniaxial compression. According to the research of Pan et al. [49], r can be taken as 1.2.

The dimensionless parameter β and effective cohesive force c are functions of the hardening parameter, expressed as

$$\beta(\boldsymbol{\kappa}) = \frac{\sigma^-(\kappa^-)}{\sigma^+(\kappa^+)}(1-\alpha) - (1+\alpha) \tag{49}$$

$$c(\boldsymbol{\kappa}) = \sigma^-(\kappa^-) \tag{50}$$

Substituting Equation (34) into Equation (33) yields

$$\dot{\boldsymbol{\sigma}} = \mathbb{E}_0 : (\dot{\boldsymbol{\varepsilon}} - \dot{\lambda}^p \frac{\partial F^p}{\partial \boldsymbol{\sigma}}) \tag{51}$$

According to the plastic consistency condition $\dot{F} = 0$ and combined with Equation (35), we have

$$\dot{\lambda}^p = \frac{\frac{\partial F}{\partial \boldsymbol{\sigma}} : \mathbb{E}_0 : \dot{\boldsymbol{\varepsilon}}}{\frac{\partial F}{\partial \boldsymbol{\sigma}} : \mathbb{E}_0 : \frac{\partial F^p}{\partial \boldsymbol{\sigma}} - \frac{\partial F}{\partial \boldsymbol{\kappa}} \cdot \mathbf{H}} \tag{52}$$

This can be obtained by bringing Equation (45) into (38)

$$\dot{\boldsymbol{\varepsilon}}^p = \dot{\lambda}^p(\alpha^p \mathbf{1} + \frac{\mathbf{s}}{\|\mathbf{s}\|}) \tag{53}$$

where $\boldsymbol{s}$ is the deviatoric stress tensor.

Substituting Equation (48) into Equation (24) yields

$$\psi_0{}^{p-} = \frac{b}{2E_0}(3J_2{}^- + \eta^p I_1^- \sqrt{3J_2} - \frac{1}{2}I_1^+ I_1^-) \tag{54}$$

The result can be expressed as [50]

$$\psi_0{}^{p-} = \frac{b}{2E_0}(3J_2{}^- + \eta^p I_1^- \sqrt{3J_2} - \frac{1}{2}I_1^+ I_1^-) \tag{55}$$

where $\eta^p = \sqrt{\frac{3}{2}}\alpha^p$ is the equivalent plastic dilatancy parameter, and $b = \frac{4}{3}\frac{\lambda^p E_0}{\|\mathbf{s}\|}$ is the material parameter. Substituting Equations (55) and (36) into (34) yields

$$Y^- = \frac{1}{2b_0}[3J_2{}^- + b_1 I_1{}^- \sqrt{3J_2{}^-} + b_2(I_1{}^-)^2 + b_3 I_1{}^- I_1{}^+] \tag{56}$$

In the formula, the coefficients b_0, b_1, b_2, b_3, respectively, are

$$\begin{aligned}
b_0 &= \frac{3E_0}{3c+2(1+\nu)} \\
b_1 &= \frac{3c\eta^p}{3c+2(1+\nu)} \\
b_2 &= \frac{1-2\nu}{3c+2(1+\nu)} \\
b_3 &= -\frac{1.5c+3\nu}{3c+2(1+\nu)}
\end{aligned} \tag{57}$$

where the parameter c is

$$c = \frac{1 - 2(1-\nu)\left(\frac{f_{b0}{}^-}{f_0{}^-}\right)^2}{(1 - 2\eta^p)\left(\frac{f_{b0}{}^-}{f_0{}^-}\right)^2 - (1 - \eta^p)} \tag{58}$$

Generally, the shear-up parameter is believed to have less influence on the multidimensional damage. If we take $\alpha^p = 0.2$, it can be expressed as follows:

$$Y^- = b_0(\alpha I_1 + \sqrt{3J_2})^2 \tag{59}$$

$$Y^+ = \psi_0{}^{e+} = \frac{1}{2}\boldsymbol{\sigma}^+ : \mathbb{C} : \boldsymbol{\sigma}^+ = \frac{1}{2E_0}\left\{\frac{2(1+\nu)}{3}3J_2{}^+ + \frac{1-2\nu}{3}(I_1{}^+)^2 - \nu I_1{}^+ I_1{}^-\right\} \tag{60}$$

where b_0 is the material parameter and ν is Poisson's ratio.

The expression for plastic HEF is formulated based on the aforementioned theory. In practical applications, calculating plastic deformation can employ a simple empirical model. Considering the coupling of plasticity and damage, Li and Ren [47] proposed a plastic evolution model:

$$\boldsymbol{\varepsilon}^p = \mathbb{E}^{-1} : \mathbb{F} : \mathbb{E} : \boldsymbol{\varepsilon} \tag{61}$$

Here, $\mathbb{F}$ is a fourth-order tensor, and takes the form:

$$\mathbb{F} = \zeta_p{}^+ d^+ \mathbb{P}^+ + \zeta_p{}^- d^- \mathbb{P}^- \tag{62}$$

where $\zeta_p{}^\pm$ is the plastic parameter, and $\mathbb{P}^+, \mathbb{P}^-$ are given by Equation (16).

According to the thermodynamic theory, the damage evolution function can be defined as

$$d^\pm = g_Y{}^\pm(Y^\pm) \tag{63}$$

The explicit form of the g_Y is more difficult to give. Still, due to the monotonically increasing nature of the damage, there is indeed a one-to-one mapping relationship between g_Y and Y. If the initial damage state and the energy release rate remain consistent during the damage process for two stress states. The damage to the material will be the same at the end of the process. This applies regardless of whether the material is in a one-dimensional or multidimensional stress state. This is known as the damage consistency condition.

Based on the damage consistency condition, for a given set of principal elastic strains $(\varepsilon_1^e, \varepsilon_2^e, \varepsilon_3^e)$, we can determine a uniaxial strain $\bar{\varepsilon}^e$, which can be made so that the damage variables are equal at both sets of strains. This strain is the energy equivalent strain.

2.3.5. Deduction to the One-Dimensional Case

For uniaxial loading, whether under tension or compression, there is only one scalar strain ε, and the undamaged material is a linear elastic material. The constitutive model constructed by uniaxial loading is an elastic damage model, such as

$$\varepsilon^e = \varepsilon \tag{64}$$

$$\sigma = E\varepsilon \tag{65}$$

Making the uniaxial loading energy release rate equal to the three-dimensional stress energy release rate, we have

$$\bar{\varepsilon}^{e-} = \frac{1}{E(1-\alpha)}\sqrt{\frac{Y^-}{b_0}} \tag{66}$$

$$\bar{\varepsilon}^{e+} = \sqrt{\frac{Y^+}{2E}} \tag{67}$$

Substituting the equivalent energy strain into Formulas (4) and (7) yields:

$$d^\pm = d^\pm(\bar{\varepsilon}^{e\pm}) \tag{68}$$

After obtaining the principal direction damage variable, the *i*-th actual principal stress tensor can be obtained as

$$\widetilde{\boldsymbol{\sigma}}_p^\pm = (1-d^\pm) : \boldsymbol{\sigma}_p^\pm \tag{69}$$

$$\widetilde{\boldsymbol{\sigma}}_p = \widetilde{\boldsymbol{\sigma}}_p^+ + \widetilde{\boldsymbol{\sigma}}_p^- \tag{70}$$

According to the actual principal stress tensor, the stress tensor can be obtained as

$$\widetilde{\boldsymbol{\sigma}} = \mathbf{Q}\widetilde{\boldsymbol{\sigma}}_{\mathbf{p}}\mathbf{Q}^T \tag{71}$$

At this point, the three-dimensional constitutive model has been established, and the specific process is shown in Figure 8. After determining the equivalent strain, the three-dimensional ontological relationship can be established using a standard procedure. This offers a powerful tool for analyzing and predicting the mechanical behavior of ECCS under complex stress states.
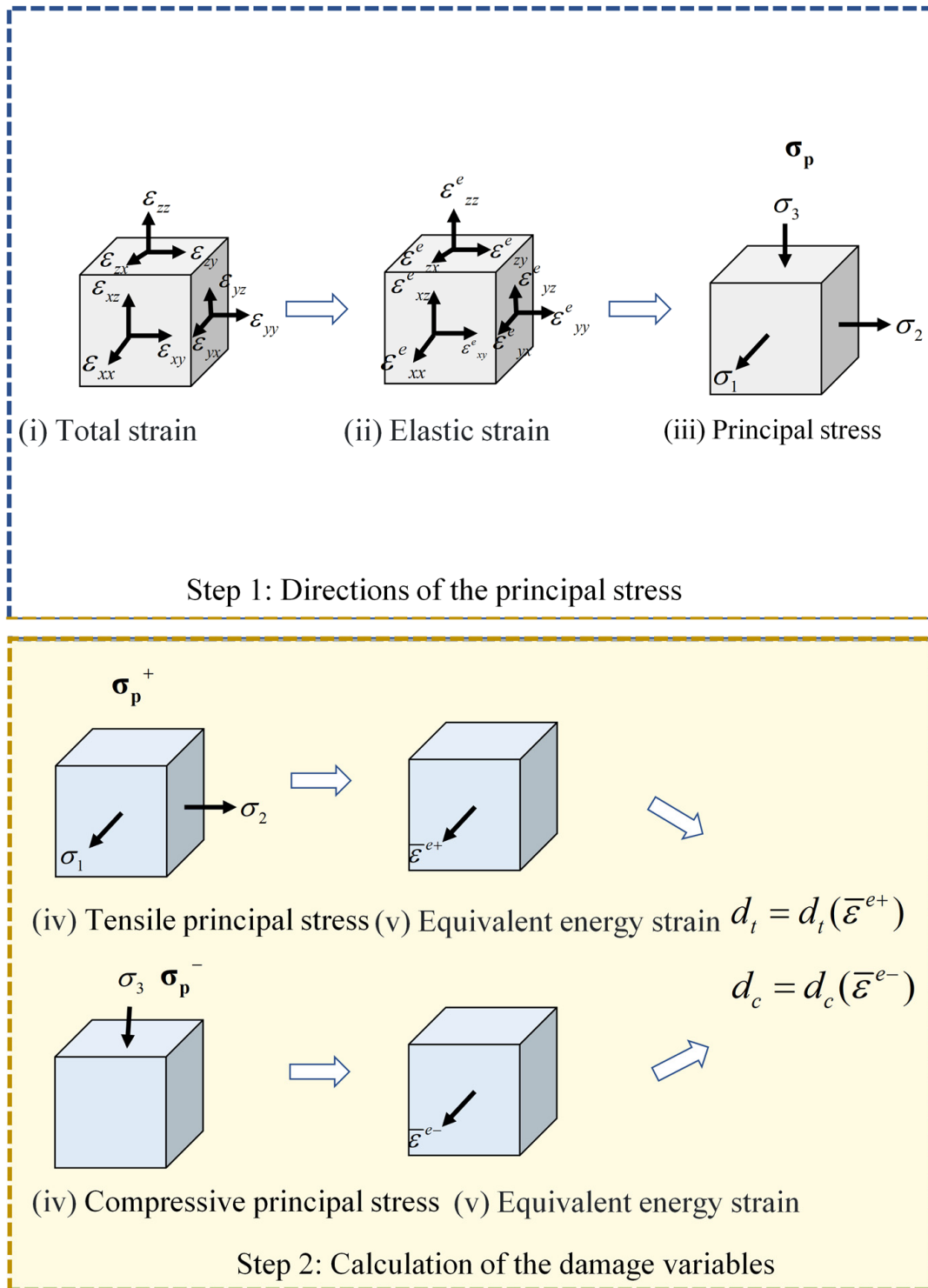
Figure 8. *Cont.*
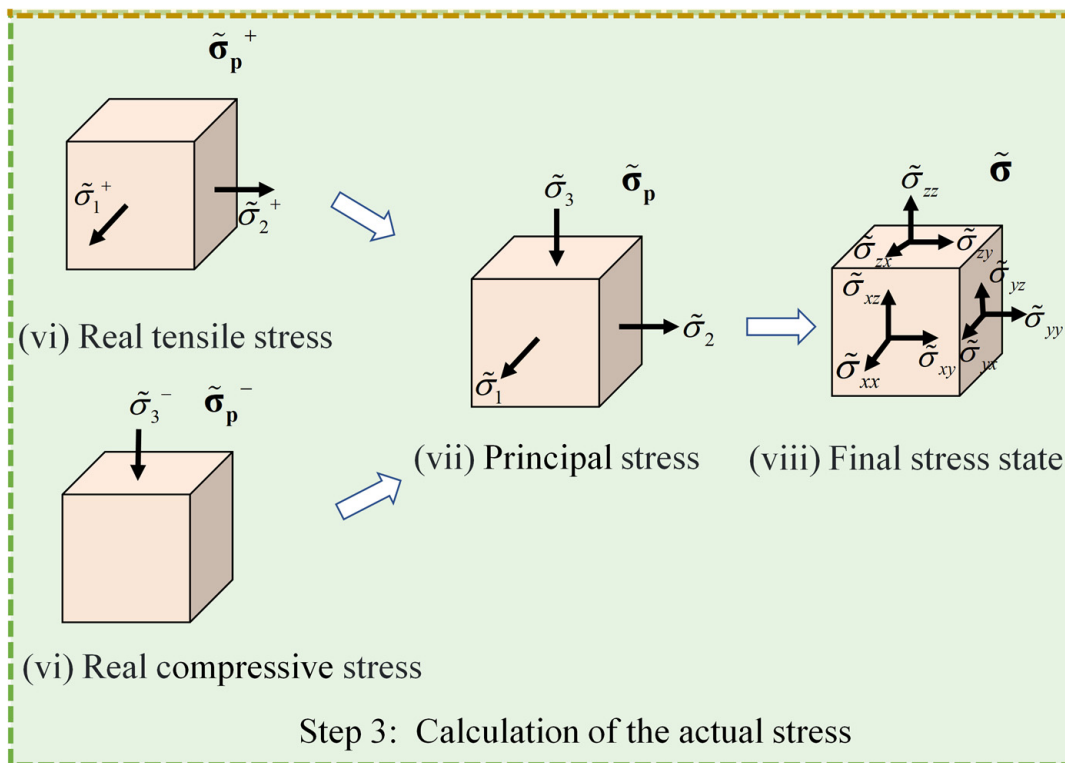
Figure 8. Three steps for establishing three-dimensional constitutive relationships.

3. Subroutines for the ECCs Constitutive Model

3.1. Secondary Development of VUMAT Subroutines

ABAQUS has built-in interfaces to user material subroutines, UMAT and VUMAT, enabling users to use material models not defined in the ABAQUS material library. Both have the same functionality and are suitable for different analyses: the UMAT subroutine for implicit analysis and the VUMAT subroutine for explicit analysis [51].

Due to the softening phase, also known as the negative tangent stiffness phenomenon, in the constitutive relationship Equation (2), using the UMAT subroutine leads to convergence difficulties. As a result, this paper utilizes the VUMAT subroutine for programming and numerical simulation during a quasi-static process.

The primary goal of writing the VUMAT subroutine is to calculate the stress matrix using the strain increment and the initial stress matrix. There are two methods: the incremental method and the full method [52].

The incremental method is expressed as

$$\sigma_{i+1} = \sigma_i + f(\Delta\varepsilon) \tag{72}$$

where σ_i is the stress matrix at the beginning of the incremental step, $\Delta\varepsilon$ is the strain increment of the incremental step, and σ_{i+1} is the stress matrix at the end of the incremental step.

The full-measurement method is simply expressed as

$$\varepsilon_{i+1} = \varepsilon_i + \Delta\varepsilon \tag{73}$$

$$\sigma_{i+1} = f(\varepsilon_{i+1}) \tag{74}$$

where ε_i is the strain matrix at the beginning of the incremental step, $\Delta\varepsilon$ is the strain increment of the incremental step, ε_{i+1} is the strain matrix at the end of the incremental step, and σ_{i+1} is the strain matrix at the end of the incremental step.

The specific process is as follows:

(1) Calculate elastic test stress:

$$\boldsymbol{\sigma}^{tr} = \mathbb{E} : \boldsymbol{\varepsilon} \tag{75}$$

(2) Calculate the principal stress and decompose the test stress:

$$\boldsymbol{\sigma}^{tr-} = \mathbf{Q}\boldsymbol{\sigma}_{\mathrm{P}}^{tr-}\mathbf{Q}^T \text{and } \boldsymbol{\sigma}^{tr+} = \mathbf{Q}\boldsymbol{\sigma}_{\mathrm{P}}^{tr+}\mathbf{Q}^T \tag{76}$$

(3) Calculate energy release rate:

$$Y^{\pm} = Y^{\pm}(\boldsymbol{\sigma}^{tr+}, \boldsymbol{\sigma}^{tr-}) \tag{77}$$

(4) Calculate equivalent energy strain and damage variables:

$$\bar{\varepsilon}^{e\pm} = \bar{\varepsilon}^{e\pm}(Y^{\pm}) \tag{78}$$

$$d^{\pm} = d^{\pm}(\bar{\varepsilon}^{e\pm}) \tag{79}$$

(5) Perform plastic correction, substitute into Equation (61) to correct the strain, and return to step (1) to recalculate the stress–strain and damage variables until:

$$d_{i+1} - d_i < \delta \tag{80}$$

where δ is the given result accuracy.

(6) Calculate the true stress based on the damage variable and stress:

$$\widetilde{\boldsymbol{\sigma}}_p^{\pm} = (1 - d^{\pm}) : \boldsymbol{\sigma}_p^{\pm} \tag{81}$$

$$\widetilde{\boldsymbol{\sigma}}_p = \widetilde{\boldsymbol{\sigma}}_p^+ + \widetilde{\boldsymbol{\sigma}}_p^- \tag{82}$$

$$\widetilde{\boldsymbol{\sigma}} = \mathbf{Q}\widetilde{\boldsymbol{\sigma}}_{\mathbf{p}}\mathbf{Q}^T \tag{83}$$

3.2. Uniaxial Tension/Compression

When performing finite element analysis or other numerical methods for validation, it is important to consider cell dependence. To address this, a single element is used for validation to avoid the issues caused by too many units. The same test data as in Sections 2.1 and 2.2 are used, and the values of the relevant parameters are taken from Table 7. For simplicity, plastic deformation is assumed to be negligible.

Table 7. Values of parameters required for numerical simulation and their definitions.

Parameter	Value	Significance
Density (10^3 kg/mm^3)	2.3×10^{-9}	Density
Depvar	20	State variable
E (MPa)	9027.63	Young's modulus
ν	0.18	Poisson's ratio
σ_{cr} (MPa)	46.45	Peak stress in compression
ε_{cr}	0.006042	Strain corresponding to peak stress in compression
σ_{tr} (MPa)	3.1121	Inflection point stress in tension
ε_{tr}	0.00045	strain corresponding to inflection point stress in tension
σ_{tp} (MPa)	4.4989	Breaking point stress in tension
ε_{tp}	0.03333467	strain corresponding to breaking point stress in tension
α_c	1.391	Damage variable parameters, obtained through fitting
γ_c	1.443	Damage variable parameters, obtained through fitting
r	1.2	Damage variable parameters, Taken from the convention

Analysis step and boundary conditions: the dynamic explicit analysis is selected, the constraints are selected as three adjacent faces normal to the constraints, the load form is

displacement control on one side, and the strain is 0.05. The model and meshing are shown in Figure 9.

(a)   **(b)**
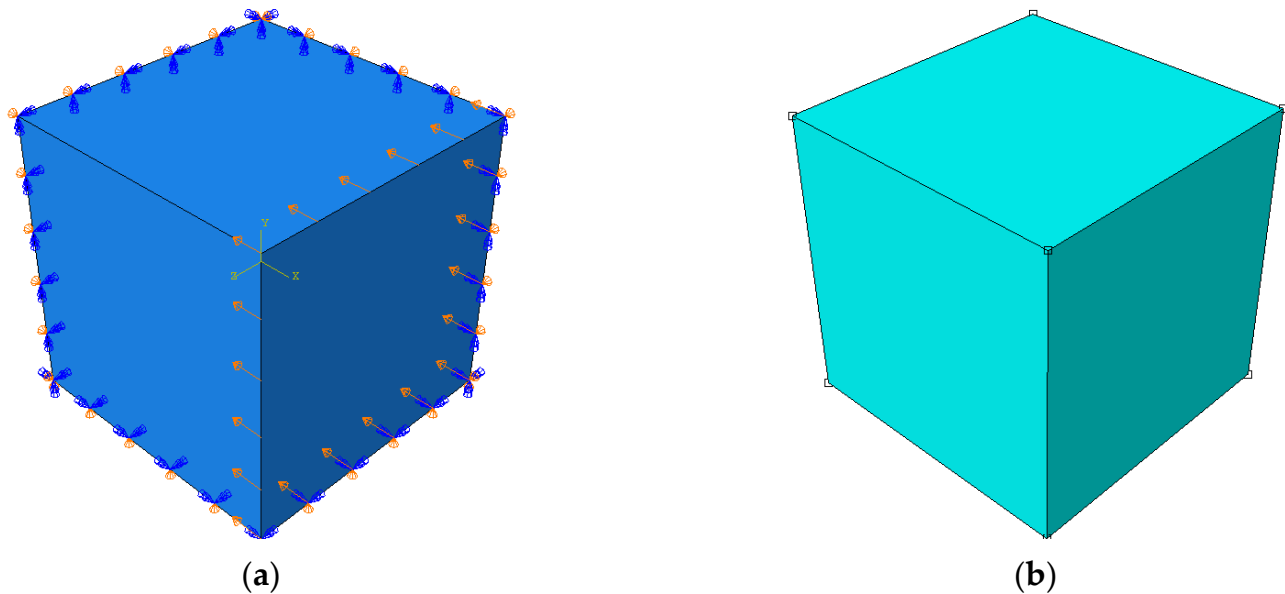
Figure 9. Simulation of the uniaxial loading of a single element: (**a**) boundary condition; (**b**) meshing of the single element.

3.2.1. Uniaxial Compression

Figure 10 illustrates the strains in the material under uniaxial compression with different stress levels. Red dots represent the test data for uniaxial compression, while the solid black lines indicate the results of finite element calculations. Specifically, we chose to display the stress contour at a strain of 0.03. The graphs indicate that the test data and the finite element calculation results agree well before reaching the peak stress. They exhibit the same stiffness before reaching the peak stress and strain and largely overlap in the material softening stage. Overall, the fitting error between the test data and the finite element calculation data is less than 2%, demonstrating that the written subroutine is reliable for uniaxial compression. This subroutine can also be applied to more complex loading conditions and material behavior analysis.

3.2.2. Uniaxial Tension

Figure 11 demonstrates the variation in tensile stress with tensile strain under uniaxial tension conditions. From the figure, it can be seen that before the material reaches the inflection point of the dense crack stage, the finite element solution maintains a good agreement with the stiffness demonstrated by the test data, i.e., both of them have similar proportionality between stress and strain, which proves the accuracy of the finite element model in simulating the elastic behavior of the material. Meanwhile, when the material enters the inflection point of the dense cracking stage, the finite element solution and the test data overlap in terms of stress values, which further validates the reliability of the finite element analysis in predicting the material damage point. However, as the strain increases further and the material enters the dense crack stage, the test data fluctuate due to the effects of fiber breakage and pullout, etc., and the finite element solution and the test data may deviate from each other numerically to a certain extent. Nevertheless, the overall trends of the two remain consistent, further indicating that the finite element model can still effectively capture the mechanical behavior of the material in the dense crack stage despite the numerical deviation.
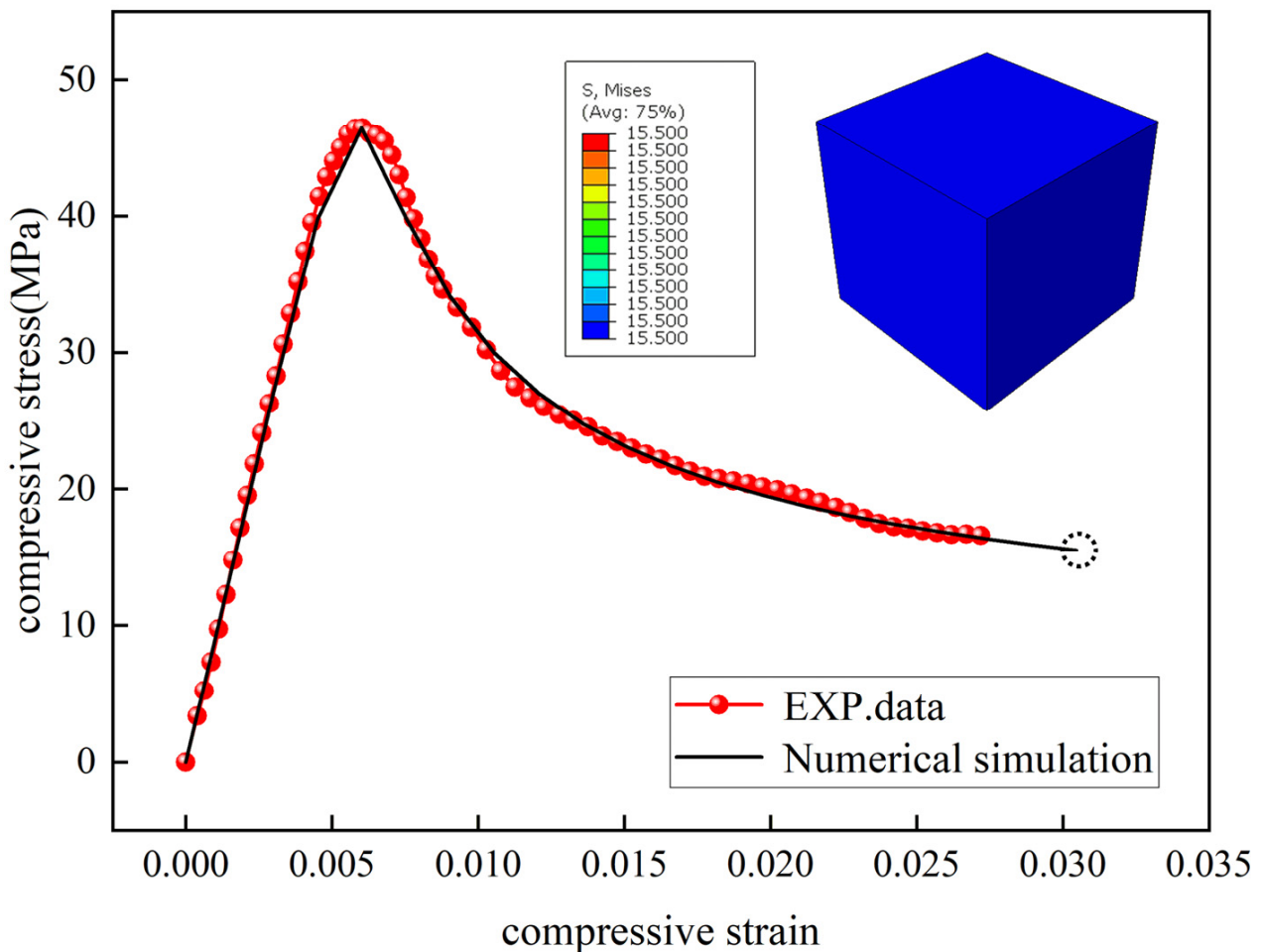
Figure 10. Comparison between numerical and experimental stress–strain curves of ECCs under uniaxial compression. The blue cube represents the stress contour of the compressive ECCs at strain 0.03.

In summary, Figure 11 fully demonstrates the good agreement between the finite element solution and the experimental data under uniaxial tensile conditions, especially at the critical stages before and after the material damage. This provides strong support for our further analysis and research.

3.3. Four-Point Bending

ECC materials in pavement structures are primarily exposed to bending loads. As a result, assessing their bending performance is crucial to understanding their mechanical properties. The classical four-point bending test for thin plates was employed to evaluate the bending performance of ECCs.

As shown in Figure 12a, the dimensions of the ECC specimens used in the test are 350 mm × 50 mm × 15 mm thin plate specimens. The four-point bending test loaded the specimen, and the loading rate was set at 0.5 mm/min. To comprehensively record the deformation process and cracking of the ECC materials under bending load, the XTDIC system was utilized for the real-time observation and collection of the deflection of the specimen in the span. At the same time, the force transducer that comes with the testing machine was used to measure the change of load, and the specific four-point bending test setup is shown in Figure 12b.
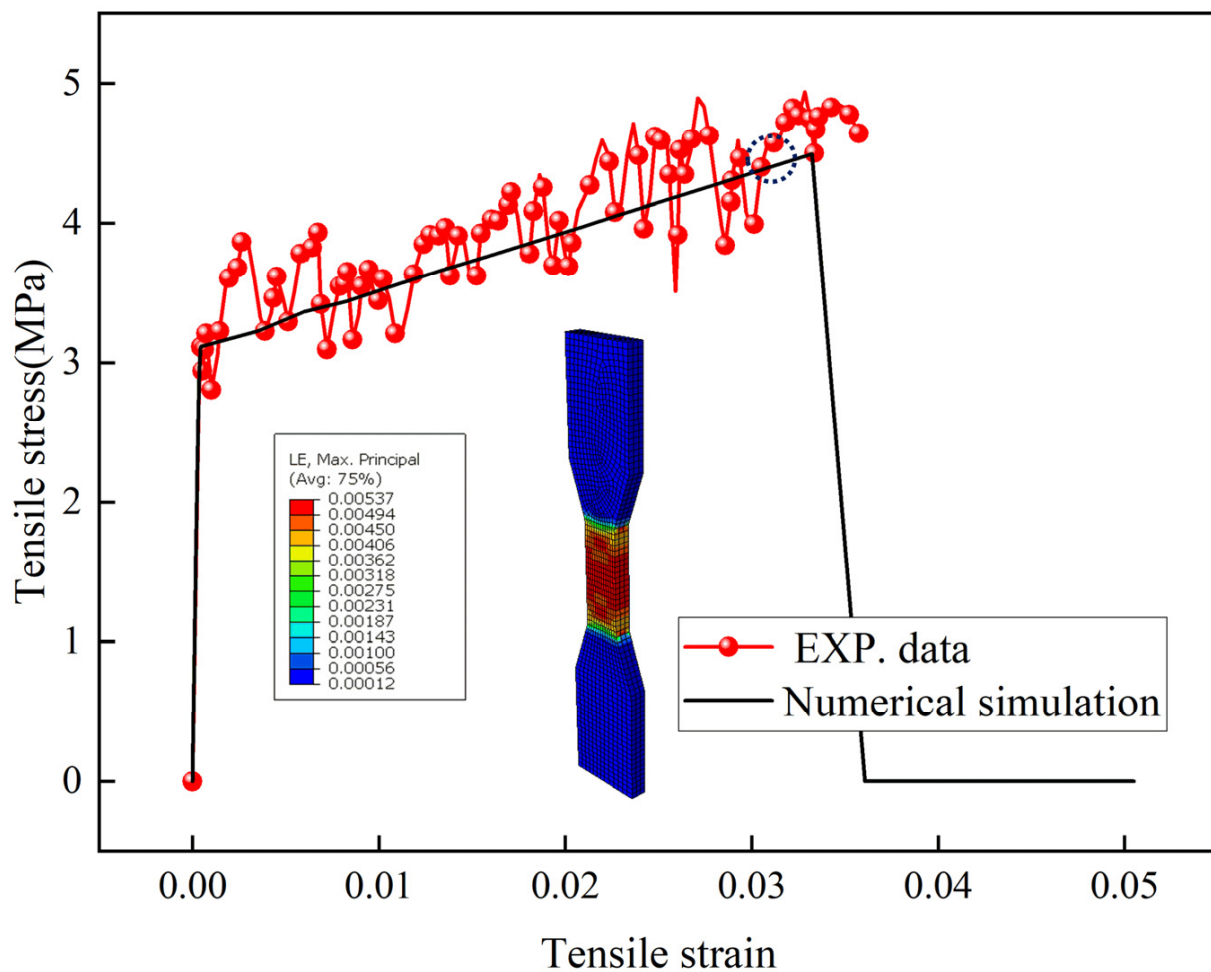
Figure 11. Comparison between numerical and experimental stress–strain curves of ECCs under uniaxial tension.

The test data for the four-point bending test were chosen to match the ECCs used in the uniaxial tensile test. This allowed for the calculation of tensile stresses on the bottom surface. In the model depicted in Figure 12a, the bending moment equation for the thin plate is $M = \frac{Px}{2}$ for $0 \leq x \leq L/3$ and $M = \frac{PL}{6}$ for $L/3 \leq x \leq L/2$, where P is the load, and L is the distance between supports.

In the context of purely bending beams, the bending tensile stress at the center of the bottom surface of the four-point bend is determined according to ASTM C1609-19a [53] (Standard Test Method for Flexural Properties of Fiber-Reinforced Concrete), namely $\sigma_t = \frac{PL}{bh^2}$, where b is the section width, and h is the section height.

In the modeling process, a quarter centrosymmetric model was selected for the study, as shown in Figure 13, with the same parameter settings as the uniaxial tension test. For the boundary conditions, the two cylinders are set as rigid bodies, the contact mode is hard contact, and the friction coefficient is set to 0.1. Fixed constraints are applied to the supporting cylinders, while symmetric constraints are applied to the tangential surfaces. For the displacement boundary conditions, the loaded cylinders were loaded by applying displacements in the negative direction of the *Y*-axis at the critical points on the loaded cylinders. A six-layer mesh in the thickness direction was chosen to improve the simulation accuracy, and the C3D8R cell type was used.
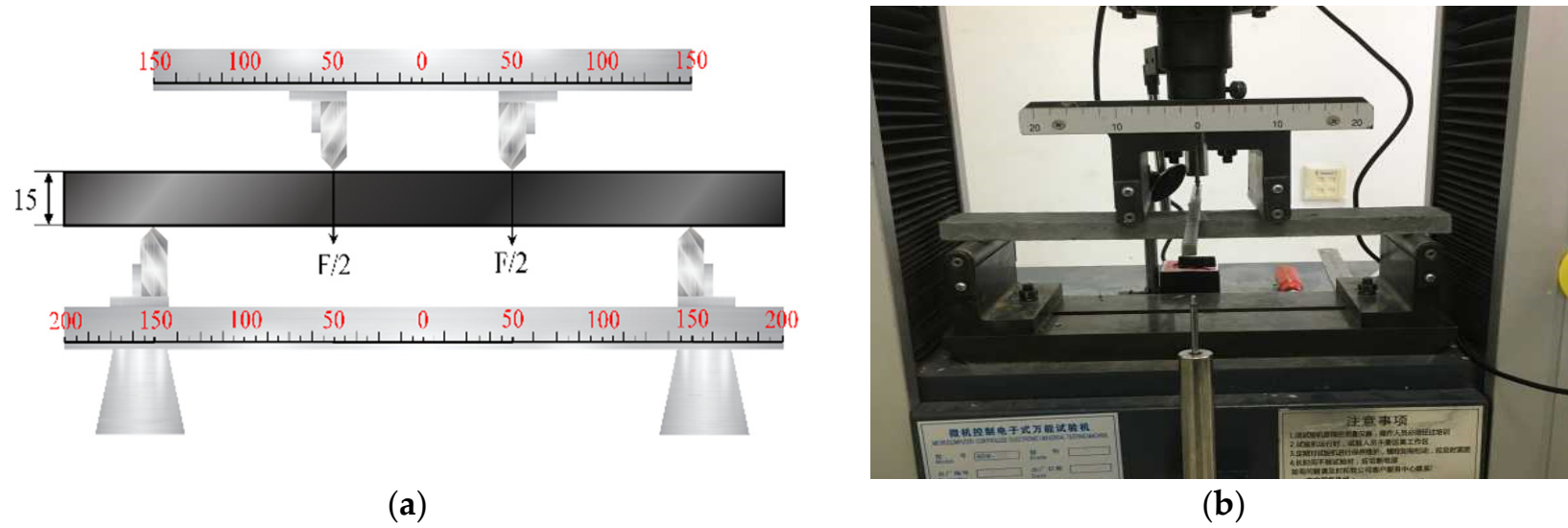
Figure 12. Four-point bending test diagram: (**a**) schematic diagram; (**b**) diagram of the device.
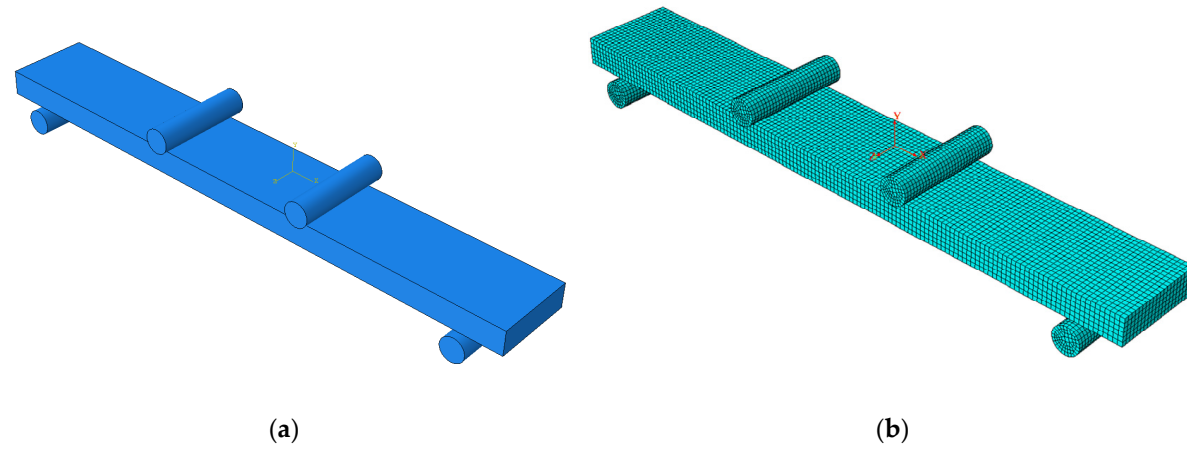
Figure 13. Four-point bending simulation diagram: (**a**) modeling; (**b**) meshing.

Figure 14 represents the variation in tensile stress with center deflection for a thin plate in four-point bending. At the initial stage, it can be found that the stiffness of the test data is slightly larger than that of the finite element solution. When the tensile stress reaches 6 MPa, the deflection shown by the test data is only 0.3 mm, while the deflection demonstrated by the finite element solution reaches 1.4 mm. On the contrary, after entering the hardening stage, the strength of the finite element solution is slightly larger than that of the test data, but the difference between the two stays within the error range of about 7%. The trend of the test data and the finite element solution is consistent regarding the overall trend, indicating that the model is more accurate in its simulation ability at this stage. Such an error is considered acceptable, considering that there may be some gaps in the material properties of different ratios.
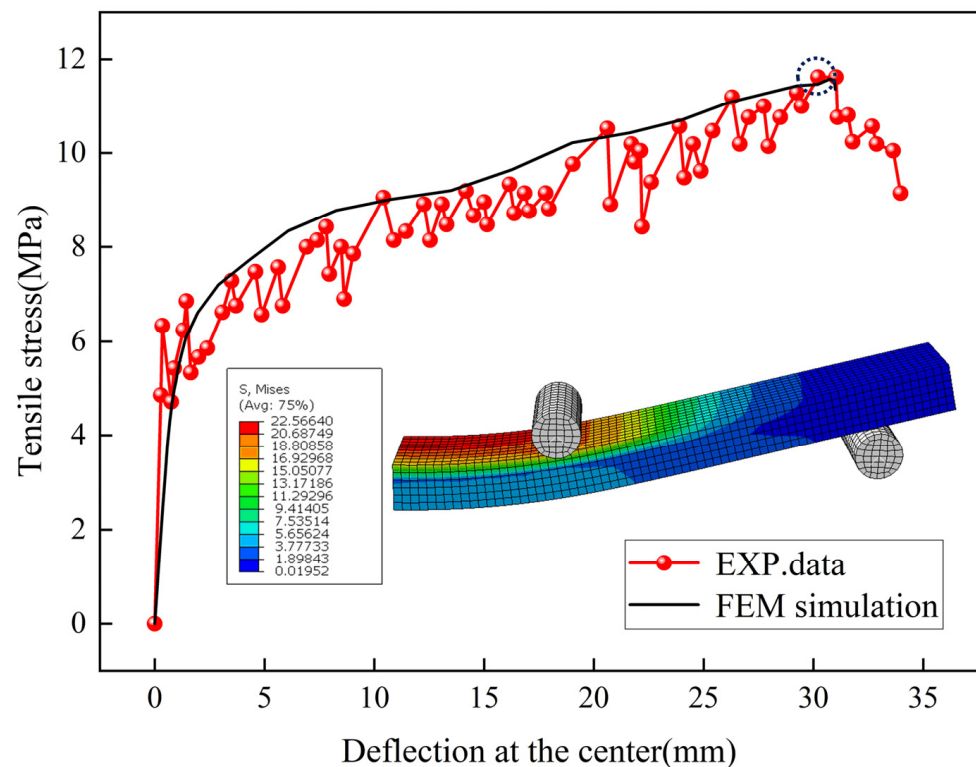
Figure 14. Comparison between numerical and experimental bending tensile stress–deflection curves under a four-point bending test.

In summary, the four-point bending simulation serves as a validation model to demonstrate the reliability of the three-dimensional intrinsic model of the subroutine. After obtaining the test parameters of ECC materials under specific ratios, the model can effectively simulate their structural stress response in practical engineering applications, providing solid theoretical support for applying ECC materials in engineering fields.

4. Conclusions

The current lack of an effective constitutive model to accurately describe the mechanical behavior of ECCs under multiaxial loading and deformation is a pressing issue. This paper addresses this problem by introducing a damage variable function based on experimental uniaxial tension and compression data. A one-dimensional damage theoretical model is established to reflect the mechanical behavior of ECCs in uniaxial loading accurately. Additionally, the paper introduces the energy release rate and energy equivalent strain based on the principle of damage mechanics, extending the one-dimensional model to a three-dimensional ECC constitutive model. This three-dimensional model effectively reflects the damage behavior of ECC materials and the interactions between various di-

rections under multiaxial stresses. Finally, the constitutive relationship is embedded into ABAQUS through the VUMAT subroutine, and the simulation results of uniaxial tension and compression, as well as four-point bending, are compared with the test. This process verifies the validity of the constitutive model, solves the finite element simulation problem of ECC-containing structures, and provides a solid theoretical basis and design guidance for engineering applications and structural optimization. In the future, it is recommended that research focus on contact and cyclic loading experiments of reinforced engineered cementitious composite (ECC) structures to better reflect actual engineering conditions. These studies can further investigate the performance characteristics and service life of ECC structures, ultimately enhancing the reliability of numerical simulation results.

Author Contributions: Conceptualization: S.Y.; methodology: S.Y.; software: Y.L. (lead) and X.W. (supporting); formal analysis: T.D. (lead) and Z.W. (supporting); investigation: T.D.; data curation: X.W. (lead) and T.S. (supporting); writing—original draft: T.D. (lead) and Z.W. (supporting); writing—review and editing: S.Y. All authors have read and agreed to the published version of the manuscript.

Data Availability Statement: The data that support the findings of this research work are available from the corresponding author, Shengyou Yang, upon reasonable request.

Conflicts of Interest: Although the author Tingting Ding, Zhuo Wang and Yang Liu were employed by the company Shandong Provincial Communications Planning and Design Institute Group Co., Ltd., Xinlong Wang, Tingxin Sun and Shengyou Yang declare that the research was conducted in the absence of any commercial or financial relationships that could be construed as a potential conflict of interest. The company had no role in the design of the study; in the collection, analyses, or interpretation of data; in the writing of the manuscript, or in the decision to publish the results.

References

1. Shoji, D.; He, Z.; Zhang, D.; Li, V.C. The greening of engineered cementitious composites (ECC): A review. *Constr. Build. Mater.* **2022**, *327*, 126701. [CrossRef]
2. Afroughsabet, V.; Biolzi, L.; Ozbakkaloglu, T. High-performance fiber-reinforced concrete: A review. *J. Mater. Sci.* **2016**, *51*, 6517–6551. [CrossRef]
3. Siddika, A.; Al Mamun, A.; Alyousef, R.; Amran, Y.M. Strengthening of reinforced concrete beams by using fiber-reinforced polymer composites: A review. *J. Build. Eng.* **2019**, *25*, 100798. [CrossRef]
4. Grzesiak, S.; Pahn, M.; Schultz-Cornelius, M.; Bies, N.S. Influence of different fiber dosages on the behaviour of Façade anchors in high-performance concrete. *CivilEng* **2021**, *2*, 556–579. [CrossRef]
5. Shah, S.J.; Naeem, A.; Hejazi, F.; Mahar, W.A.; Haseeb, A. Experimental Investigation of Mechanical Properties of Concrete Mix with Lightweight Expanded Polystyrene and Steel Fibers. *CivilEng* **2024**, *5*, 209–223. [CrossRef]
6. Mohamed, O.; Zuaiter, H. Fresh properties, strength, and durability of fiber-reinforced geopolymer and conventional concrete: A review. *Polymers* **2024**, *16*, 141. [CrossRef]
7. Li, V.; Leung, C. Theory of steady state and multiple cracking of random discontinuous fiber reinforced brittle matrix composites. *ASCE J. Eng. Mech.* **1992**, *118*, 2246–2264. [CrossRef]
8. Yu, J.; Li, V. Research on production, performance and fibre dispersion of PVA engineering cementitious composites. *Mater. Sci. Technol.* **2009**, *25*, 651–656. [CrossRef]
9. Li, M.; Li, V. Rheology, fiber dispersion, and robust properties of engineered cementitious composites. *Mater. Struct.* **2013**, *46*, 405–420. [CrossRef]
10. Ghahsareh, F.M.; Guo, P.; Wang, Y.; Meng, W.; Li, V.C.; Bao, Y. Review on material specification, characterization, and quality control of engineered cementitious composite (ECC). *Constr. Build. Mater.* **2024**, *442*, 137699. [CrossRef]
11. Hedjazi, S.; Castillo, D. Utilizing Polypropylene Fiber in Sustainable Structural Concrete Mixtures. *CivilEng* **2022**, *3*, 562–572. [CrossRef]
12. Bediwy, A.; El-Salakawy, E.F. Mechanical properties of hybrid structures incorporating nano-silica and basalt fiber pellets. *CivilEng* **2021**, *2*, 909–928. [CrossRef]
13. Paschalis, S.A.; Lampropoulos, A.P.; Tsioulou, O. Experimental and numerical study of the performance of ultra high performance fiber reinforced concrete for the flexural strengthening of full scale reinforced concrete members. *Constr. Build. Mater.* **2018**, *186*, 351–366. [CrossRef]

14. Tajasosi, S.; Saradar, A.; Barandoust, J.; Mohtasham Moein, M.; Zeinali, R.; Karakouzian, M. Multi-criteria risk analysis of ultra-high performance concrete application in structures. *CivilEng* **2023**, *4*, 1016–1035. [CrossRef]

15. Ma, K.; Ma, Y.; Liu, B. Experimental investigation on ultra high performance fiber reinforced concrete beams. *Mech. Adv. Mater. Struct.* **2023**, *30*, 1155–1171. [CrossRef]

16. Şahmaran, M.; Lachemi, M.; Hossain, K.M.; Li, V.C. Internal curing of engineered cementitious composites for prevention of early age autogenous shrinkage cracking. *Cem. Concr. Res.* **2009**, *39*, 893–901. [CrossRef]

17. Liu, W.; Xu, S.; Feng, P. Fatigue damage propagation models for ductile fracture of ultrahigh toughness cementitious composites. *Int. J. Damage Mech.* **2016**, *26*, 919–932. [CrossRef]

18. Zhang, Q.; Li, V. Development of durable spray-applied fire-resistive Engineered Cementitious Composites (SFR-ECC). *Cem. Concr. Compos.* **2015**, *60*, 10–16. [CrossRef]

19. Hou, M.; Zhang, D.; Li, V.C. Crack width control and mechanical properties of low carbon engineered cementitious composites (ECC). *Constr. Build. Mater.* **2022**, *348*, 128692. [CrossRef]

20. Tawfek, A.; Ge, Z.; Yuan, H.; Zhang, N.; Zhang, H.; Ling, Y.; Guan, Y.; Šavija, B. Influence of fiber orientation on the mechanical responses of engineering cementitious composite (ECC) under various loading conditions. *J. Build. Eng.* **2023**, *63*, 105518. [CrossRef]

21. Yang, Z.; Xiong, Z.; Liu, Y. Study on the self-recovery performance of SMAF-ECC under cyclic tensile loading. *Constr. Build. Mater.* **2024**, *392*, 131895. [CrossRef]

22. Zhu, M.; Chen, B.; Wu, M.; Han, J. Effects of different mixing ratio parameters on mechanical properties of cost-effective green engineered cementitious composites (ECC). *Constr. Build. Mater.* **2022**, *328*, 127093. [CrossRef]

23. Feng, H.; Nie, S.; Guo, A.; Lv, L.; Yu, J. Evaluation on the performance of magnesium phosphate cement-based engineered cementitious composites (MPC-ECC) with blended fly ash/silica fume. *Constr. Build. Mater.* **2022**, *341*, 127861. [CrossRef]

24. Liao, Q.; Xie, X.; Yu, J. Numerical investigation on dynamic performance of reinforced ultra-high ductile concrete–ultra-high performance concrete panel under explosion. *Struct. Concr.* **2022**, *23*, 3601–3615. [CrossRef]

25. Sui, L.; Zhong, Q.; Yu, K.; Xing, F.; Li, P.; Zhou, Y. Flexural fatigue properties of ultra-high performance engineered cementitious composites (UHP-ECC) reinforced by polymer fibers. *Polymers* **2018**, *10*, 892. [CrossRef]

26. Wu, X.; Tian, J.; Ma, H.; Zheng, Y.; Hu, S.; Wang, W.; Du, Y.; Huang, W.; Sun, C.; Zhu, Z. Investigation on interface fracture properties and nonlinear fracture model between ECC and concrete subjected to salt freeze-thaw cycles. *Constr. Build. Mater.* **2020**, *259*, 119785. [CrossRef]

27. Hossain, K.; Hossain, M.; Manzur, T. Performance of engineered cementitious composite covered or wrapped self-consolidating concrete beams under corrosion. *Eng. Struct.* **2020**, *219*, 110801. [CrossRef]

28. Zhang, Z.; Hu, J.; Ma, H. Feasibility study of ECC with self-healing capacity applied on the long-span steel bridge deck overlay. *Int. J. Pavement Eng.* **2017**, *20*, 884–893. [CrossRef]

29. Ding, Y.; Yu, K.; Mao, W. Compressive performance of all-grade engineered cementitious composites: Experiment and theoretical model. *Constr. Build. Mater.* **2020**, *244*, 118357. [CrossRef]

30. Gencturk, B.; Elnashai, A.S. Numerical modeling and analysis of ECC structures. *Mater. Struct.* **2013**, *46*, 663–682. [CrossRef]

31. Naser, S.; Hamid, R.; Abbas, Y. Effect of short to long hybrid elastic/hyperelastic (Glass/PP) fibers on high-strength engineered cementitious composites (ECC), along with presenting a constitutive model. *J. Build. Eng.* **2024**, *89*, 109215.

32. Che, J.; Guo, Z.; Yang, P.; Liu, H. Experimental investigation on seismic behavior of brick masonry wall strengthened with ECC splint. *Constr. Build. Mater.* **2023**, *391*, 131627. [CrossRef]

33. Kanda, T.; Lin, Z.; Li, V. Tensile stress-strain modeling of pseudostrain hardening cementitious composites. *J. Mater. Civ. Eng.* **2000**, *12*, 147–156. [CrossRef]

34. Zhang, C.; Yang, X. Bilinear elastoplastic constitutive model with polyvinyl alcohol content for strain-hardening cementitious composite. *Constr. Build. Mater.* **2019**, *209*, 388–394. [CrossRef]

35. Chen, S.F.; Chen, J.F.; Yang, F.X.; Liu, Z.M. Constitutive model for engineered cementitious composites under biaxial compression. *Eng. Mech.* **2020**, *37*, 87–98.

36. Pan, Z.; Qiao, Z.; Si, D.; Shang, J. Experimental investigation and numerical simulation on uniaxial tensile behavior of hybrid PVA-ECC. *Constr. Build. Mater.* **2023**, *398*, 132517. [CrossRef]

37. Luo, Q.; Lu, Z.; Wang, F.; Liu, Z.; Xin, Z.; Jiang, J. Influence of flaw distribution on tensile behavior of Engineered Cementitious Composites (ECC) based on flaw probability model. *Constr. Build. Mater.* **2023**, *402*, 133096. [CrossRef]

38. Krahl, P.A.; Carrazedo, R.; El Debs, M.K. Mechanical damage evolution in UHPFRC: Experimental and numerical investigation. *Eng. Struct.* **2018**, *170*, 63–77. [CrossRef]

39. Cai, J.; Pan, J.; Tan, J.; Vandevyvere, B. Nonlinear finite-element analysis for hysteretic behavior of ECC-encased CFST columns. *Structures* **2020**, *25*, 670–682. [CrossRef]

40. Cheng, H.; Paz, C.M.; Pinheiro, B.C.; Estefen, S.F. Experimentally based parameters applied to concrete damage plasticity model for strain harding cementitious composite in sandwich pipes. *Mater. Struct.* **2020**, *53*, 78. [CrossRef]

41. Ministry of Construction, People's Republic of China. *Code for Design of Concrete Structures*; China Construction Industry Press: Beijing, China, 2010.

42. Ministry of Housing and Urban-Rural Development of the People's Republic of China. *Standard for Test Methods of Concrete Physical and Mechanical Properties*; China Construction Industry Press: Beijing, China, 2019.

43. Lemaitre, J.; Desmorat, R. *Engineering Damage Mechanics*; Springer: Berlin/Heidelberg, Germany, 2005; pp. 16–18. [CrossRef]

44. Ladevèze, P. On an anisotropic damage theory, failure criteria of structured media. In Proceedings of the CNRS International Colloquium, Villard-de-Lans, France, 21–24 June 1983.

45. Mazars, J. Application de la Mecanique de Lendom Mangement au Comportement non Lineaire et a la Rupture du Beton de Structure. Ph.D. Thesis, Universite Paris, Paris, France, 1984.

46. Ferretti, E. Experimental procedure for verifying strain-softening in concrete. *Int. J. Fract.* **2004**, *126*, L27–L34. [CrossRef]

47. Li, J.; Ren, X. Stochastic damage model for concrete based on energy equivalent strain. *Int. J. Solids Struct.* **2009**, *46*, 2407–2419. [CrossRef]

48. Lemaitre, J. A continuous damage mechanics model for ductile fracture. *J. Eng. Mater. Technol.* **1985**, *107*, 83–89. [CrossRef]

49. Pan, J.; He, J.; Wang, L.; Zhou, J. Experimental study on mechanical behaviors and failure criterion of engineered cementitious composites under biaxial compression. *Eng. Mech.* **2016**, *33*, 186–193.

50. Wu, J.; Li, J. A new energy-based elastoplastic damage model for concrete. In Proceedings of the XXI International Conference of Theoretical and Applied Mechanics (ICTAM), Warsaw, Poland, 15–21 August 2004.

51. Zhuang, Z.; Zhang, F.; Cen, S. *ABAQUS Nonlinear Finite Element Analysis with Examples*; Science Press: Beijing, China, 2005.

52. Kan, Q.; Kang, G.; Xu, X. *Implementation of Nonlinear Constitutive Relationships in ABAQUS*; Science Press: Beijing, China, 2019.

53. Astm, C.C. *Standard Test Method for Flexural Performance of Fiber-Reinforced Concrete (Using Beam with Third-Point Loading)*; ASTM: West Conshohocken, PA, USA, 2012.